Biomolecule-assisted synthesis of $In(OH)_3$ nanocubes and In_2O_3 nanoparticles: photocatalytic degradation of organic contaminants and CO oxidation

2015 Nanotechnology 26 485601

(http://iopscience.iop.org/0957-4484/26/48/485601)

IOP Publishing Nanotechnology
Nanotechnology 26 (2015) 485601 (12pp) doi:10.1088/0957-4484/26/48/485601

Biomolecule-assisted synthesis of $In(OH)_3$ nanocubes and In_2O_3 nanoparticles: photocatalytic degradation of organic contaminants and CO oxidation

Arpan Kumar Nayak[1], **Seungwon Lee**[2], **Youngku Sohn**[2] **and Debabrata Pradhan**[1]

[1] Materials Science Centre, Indian Institute of Technology, Kharagpur 721 302, W.B., India
[2] Department of Chemistry, Yeungnam University, Gyeongsan 712-749, Korea

E-mail: youngkusohn@ynu.ac.kr and deb@matsc.iitkgp.ernet.in

Received 23 July 2015, revised 1 October 2015
Accepted for publication 13 October 2015
Published 6 November 2015

Abstract

The synthesis of nanostructured materials without any hazardous organic chemicals and expensive capping reagents is one of the challenges in nanotechnology. Here we report on the L-arginine (a biomolecule)-assisted synthesis of single crystalline cubic $In(OH)_3$ nanocubes of a size in the range of 30–60 nm along the diagonal using hydrothermal methods. Upon calcining at 750 °C for 1 h in air, $In(OH)_3$ nanocubes are transformed into In_2O_3 nanoparticles (NPs) with voids. The morphology transformation and formation of voids with the increase of the calcination temperature is studied in detail. The possible mechanism of the voids' formation is discussed on the basis of the Kirkendall effect. The photocatalytic properties of $In(OH)_3$ nanocubes and In_2O_3 NPs are studied for the degradation of rhodamin B and alizarin red S. Furthermore, the CO oxidation activity of $In(OH)_3$ nanocubes and In_2O_3 NPs is examined. The photocatalytic and CO oxidation activity are measured to be higher for In_2O_3 NPs than for $In(OH)_3$ nanocubes. This is attributed to the lower energy gap and higher specific surface area of the former. The present green synthesis has potential for the synthesis of other inorganic nanomaterials.

S Online supplementary data available from stacks.iop.org/NANO/26/485601/mmedia

Keywords: green synthesis, CO oxidation, photocatalysts

(Some figures may appear in colour only in the online journal)

1. Introduction

Semiconducting oxide nanostructures, an important class of inorganic materials, have received enormous attention in the last couple of decades because of their unique physical and chemical properties [1, 2]. The size, shape, crystal structure, and composition of nanostructures play a crucial role in their properties and performance in potential applications such as catalysis, sensors, drug-delivery, and solar cells [3–6]. For the synthesis of oxide nanomaterials, solution-based techniques such as hydrothermal, solvothermal, sol-gel, and electrochemical deposition are widely employed because of their simplicity, cost-effectiveness, greater control upon varying synthesis temperatures, precursors and their concentrations, and shape-controlling reagents [7–9]. In aqueous solution-based synthesis, the formation of hydroxide is very common and in a few applications, hydroxides have been reported to exhibit improved performance than that of their oxides [10, 11]. In particular, Yan *et al* recently reported a much higher photocatalytic activity and durability of $In(OH)_3$ than that of In_2O_3 and TiO_2 under UV light irradiation [10]. This was attributed to the strong oxidation capability, abundant surface hydroxyl groups, and large Brunauer–Emmett–Teller (BET) surface area, as well as the porous texture of $In(OH)_3$ nanocrystals. As

$In(OH)_3$ is a wide band gap semiconductor with a direct band gap energy of 5.15 eV, it does not appear attractive for photocatalytic applications and therefore only a few photocatalysis studies have dealt with it [10–12]. In contrast, In_2O_3 is an n-type semiconductor with a much smaller direct band gap of 2.9−3.1 eV [13, 14]. Moreover, a few studies have reported on the photocatalytic activity of In_2O_3 [15, 16] and further work is therefore required to understand the photocatalytic properties of both $In(OH)_3$ and In_2O_3.

The general solution-based synthesis (solvothermal, hydrothermal, and sol-gel) of $In(OH)_3$ and In_2O_3 nanomaterials involves indium salt precursors (indium acetate/nitrate/chloride/sulfate), surfactants, reducing and shape-controlling reagents such as cetyltrimethylammonium bromide (CTAB), sodium dodecyl sulfate, sodium borohydride, amines (ethylenediamine, ethylamine, L-proline, and ammonia solution), acetic acid, oleic acid, nitric acid, cyclohexane, n-pentanol, and 1-hexanol [12, 17–21]. Several of these chemicals are expensive, toxic, and hazardous, and therefore not desirable. To our knowledge, there are only a few reported works on the biomolecule (L-cysteine and DL-asparagine)-assisted synthesis of indium sulfides and oxides [22–24]. Thus, the advantage and one of the novelties of the present work lies in the use of simple and green chemicals to synthesize indium-based nanostructures.

Unlike in previous studies, the present synthesis does not involve any toxic acid or chemicals, amine and/or organic solvent, thereby making the synthesis process completely green. In addition to indium sulfate as the indium source, we used a biomolecule, i.e. L-arginine, in an aqueous medium to synthesize the $In(OH)_3$ nanocubes. L-arginine is one of the natural amino acids primarily found in red meat, fish, dairy products, chickpeas, and nuts. Amino acids are known to play an important role in controlling the shape of inorganic nanoparticles (NPs) [25, 26]. In particular, Sasaki *et al* reported cubic-shaped $In(OH)_3$ using L-aspartic acid whereas the particles were rod-shaped in the presence of glycine or L-serine or L-lysine [27]. Duan *et al* synthesized Fe_3O_4 polyhedra hydrothermally by varying the concentration of CTAB in the L-arginine solution [28]. Hu *et al* synthesized uniform-sized silver NPs via a microwave-assisted method using L-lysine and L-arginine as the reducing agent [29]. The formation of uniform-sized NPs has been attributed to the presence of amino acids in the synthesis. Amino acids (L-alanine and L-arginine) have also been used as capping agents to passivate CdS NPs and demonstrated an increase in the band gap of CdS with an increasing concentration of amino acids [30]. This suggests the important role of amino acids in the synthesis of NPs of diverse shapes and sizes.

L-arginine has been chosen in the present study because it contains a higher number of amine groups than other amino acids. Upon its decomposition at higher temperatures, the amine group of amino acids acts as a reducing agent and also preferentially coordinates on a specific surface to control the shape of the NPs. In addition, arginine is basic in nature and provides a mild, nontoxic reaction medium [29]. A higher pH is generally known to produce a higher number of nuclei and thus NPs of a smaller size [27]. Previous studies by Hu *et al* have also confirmed that amino acids with basicity are indispensible for the synthesis of uniform silver particles, whereas other amino acids such as L-aspartic acid, L-phenylalanine and L-alanine either produce aggregates of silver nanostructures or are not able to reduce the silver ions [29]. In the present work, we demonstrate the biomolecule-assisted (L-arginine) green chemical synthesis of $In(OH)_3$ nanocubes. The as-synthesized $In(OH)_3$ nanocubes are further calcined at higher temperatures (500, 600, and 750 °C) in air to produce In_2O_3 NPs with voids. The formation of voids as a function of calcination temperatures is studied and a possible mechanism is suggested. Recently, In_2O_3 has been demonstrated as a potential material for various applications including Li-ion batteries [31], dye-sensitized solar cells [32], gas sensors [33], and anti-reflection coating [34]. In the present work, in addition to the photocatalytic activity in the degradation of rhodamin B (RhB) and alizarin red S (ARS), the CO oxidation performance of $In(OH)_3$ nanocubes and In_2O_3 NPs is demonstrated. The CO oxidation performance of as-synthesized In_2O_3 NPs with voids is found to be higher than that of recently reported In_2O_3 nanostructures (cubes, donuts, and plates) [35].

2. Experimental details

2.1. Synthesis

The precursor indium sulfate ($In_2(SO_4)_3$) (Spectrochem, India), and L-arginine ($C_6H_{14}N_4O_2$) (Loba Chemicals, India) were analytical grade and used without further purification. In a typical synthesis procedure of $In(OH)_3$ nanocubes, 0.52 g (0.025 M) $In_2(SO_4)_3$ and 0.34 g (0.05 M) L-arginine (molar ratio 1:2) were added to 40 ml distilled water and stirred for 30 min at room temperature. The resultant solution was transferred to a 50 ml Teflon-lined stainless steel autoclave. The autoclave was sealed and placed inside a muffle furnace. The furnace was heated to 200 °C with a heating rate of 5 °C min^{-1} and maintained at the same temperature for 6 h before cooling to room temperature under ambient conditions. The white precipitate which formed inside the Teflon-lined autoclave was collected by centrifuging and then repeatedly washed with distilled water and absolute ethanol. The molar ratio of indium sulfate to L-arginine (1:4, 1:2, and 1:1) was varied, keeping the other synthesis parameters fixed (reaction temperature 200 °C for 6 h) to find their optimum ratio for the formation of $In(OH)_3$ nanocubes. For comparison, a controlled synthesis was also performed without L-arginine. The as-synthesized $In(OH)_3$ nanocube powder was finally dried in a vacuum oven at 60 °C for 4 h. Then, the $In(OH)_3$ nanocube powder was calcined at different temperatures (400, 500, 600, and 750 °C) for 1 h in air and its physical properties such as morphology, microstructure and phase were investigated.

2.2. Characterization

The surface morphology of the as-prepared samples was examined using a Zeiss SUPRA 40 field emission scanning

electron microscope (FESEM). The transmission electron microscopy (TEM) study on the powder product was carried out with a TECNAI G2 TEM (FEI) operated at 200 kV. The structural properties of the as-synthesized samples were studied using a PANalytical high resolution x-ray diffractometer (XRD) PW 3040/60 operated at 40 kV and 30 mA using Cu Kα x-rays. The UV–vis absorption study was done using a Scinco Neosys 2000 UV–vis spectrophotometer for the powder samples. The thermo gravimetric analysis (TGA) of the $In(OH)_3$ nanocubes was carried out using a PerkinElmer Pyris Diamond TG-DTA under atmospheric pressure. The x-ray photoelectron spectroscopy (XPS) study was carried out with a Thermo-VG Scientific ESCALab 250 microprobe with a monochromatic Al Kα source (1486.6 eV). The effective BET surface area of the as-synthesized samples was measured using a Quantachrome ChemBET analyzer.

2.3. Photocatalysis test

The photocatalytic activity of the as-synthesized single-crystalline $In(OH)_3$ nanocubes and In_2O_3 NPs was evaluated by the photodegradation of RhB and ARS dye in an aqueous solution under 365 nm ultra violet (UV) light irradiation. A powder catalyst of 20 mg ($In(OH)_3$ nanocubes or In_2O_3 NPs) was suspended in an aqueous solution of 40 ml (10^{-5} mol L^{-1} RhB/ARS) which was continuously stirred for about 1 h in the dark to establish the adsorption-desorption equilibrium between the photocatalyst, RhB, and water. Then the catalyst and mixed dye solution was irradiated with a 12 W UV source (Philips, Poland) at a working distance of 10 cm under visible light. The concentration of RhB/ARS was monitored by using a UV−vis spectrophotometer (PerkinElmer, Lambda 750). The photocatalytic activity of P-25 TiO_2 NPs (~21 nm diameter, Sigma Aldrich) was tested for comparison.

2.4. CO oxidation

CO oxidation experiments were performed with the as-synthesized $In(OH)_3$ nanocubes and In_2O_3 NPs (obtained by calcining $In(OH)_3$ nanocubes at 750 °C) at a heating rate of 10 K min^{-1} in $CO(1.0\%)/O_2/(2.5\%)/N_2$ flow conditions with a gas-flow rate of 40 ml min^{-1}. The powder sample (10 mg) was mounted in a quartz U-tube with an inner diameter of 4 mm during the reaction. The final products (e.g. CO_2 = 48 amu and H_2O = 18 amu) were detected using an RGA200 quadrupole mass spectrometer (Stanford Research Systems, USA).

3. Results and discussion

3.1. Morphology and microstructure

Figure 1(a) shows a typical FESEM image of $In(OH)_3$ nanocubes with a size distribution of about 30−150 nm synthesized at 200 °C for 6 h using the hydrothermal technique. The inset of figure 1(a) shows a magnified image of In $(OH)_3$ nanocubes depicting the corners and edges of the cubes. These nanocubes were obtained with a 1:2 molar concentration ratio of indium sulfate to L-arginine. With a 1:1 molar ratio of indium sulfate to L-arginine, NPs of a size less than 50 nm are usually obtained (figures S1(a), (b), supporting information (SI)). By taking a higher L-arginine molar quantity (i.e. 1:4 indium sulfate to L-arginine), nanocubes of a size in the range of 10−60 nm are obtained (figures S1(c), (d), SI). This suggests that the L-arginine concentration should be at least twice that of the indium sulfate to synthesize $In(OH)_3$ nanocubes. Further study was thus carried out with $In(OH)_3$ nanocubes synthesized with a 1:2 molar concentration ratio of indium sulfate to L-arginine. Du *et al* reported $In(OH)_3$ microcubes of edge length 600−700 nm with indium acetate, acetic acid, and ethanol using a solvothermal process at 240 °C for 18 h [17]. Cao *et al* synthesized $In(OH)_3$ nanocubes using indium nitrate, L-proline, and NaOH using a hydrothermal process at 210 °C for 24 h [12]. Recently, mesoporous $In(OH)_3$ nanocubes with an average size of 200 nm were reported by Shanmugasundaram *et al* using indium chloride, ethanolamine, and poly(ethylene glycol) at 220 °C for 24 h in combination with the hydrothermal technique [36]. In addition to the use of only indium sulfate and L-arginine as precursors in the aqueous medium, the synthesis temperature and duration of the present work are respectively lower and shorter than those of earlier reports [12, 17, 36]. Upon calcining at 750 °C for 1 h in air, the morphology of the $In(OH)_3$ nanocubes was found to have transformed into that of In_2O_3 NPs as shown in figure 1(b). The diameter of these NPs was measured to be in the range of 20−60 nm, which is smaller than that of nanocubes. To gain further insights into the morphology evolution, the $In(OH)_3$ nanocubes were calcined at 400, 500, and 600 °C for 1 h in air and the results of the same are discussed below.

Figures 2(a) and (b) display the TEM images of $In(OH)_3$ nanocubes synthesized with a 1:2 molar concentration ratio of indium sulfate to L-arginine at 200 °C for 6 h. The sharp corners and edges of the cubes can clearly be observed in the TEM images. The size range of 30−60 nm across the diagonal of the nanocubes is within the values obtained in the FESEM image. The lower inset of figure 2(b) shows a high resolution TEM (HRTEM) image from a part of a nanocube with a lattice spacing of 2.85 Å, corresponding to (220) planes of cubic $In(OH)_3$. The upper inset of figure 2(b) shows a spot selected area electron diffraction (SAED) pattern suggesting the single crystalline nature of the nanocubes. Upon calcining at 400 °C for 1 h in air, the morphology of the nanocubes remains the same (figure S2(a), (b), SI) but the phase is changed to cubic In_2O_3 (shown later). These results are in agreement with a previous report on the formation of In_2O_3 nanocubes by calcining $In(OH)_3$ nanocubes at 400 °C for 1 h in air [37]. With the increase of the calcination temperature to 500 °C, a large number of smaller $In(OH)_3$ nanocubes (<50 nm) were found to have fragmented to finer, near spherical, NPs with a diameter of less than 10 nm, whereas the bigger nanocubes (>50 nm) maintained their morphology, as shown in figure 2(c). Moreover, the bigger nanocubes were found to be composed of NPs making the nanocubes polycrystalline in nature. The formation of NPs is further confirmed by the magnified TEM image (figure 2(d)) and ring

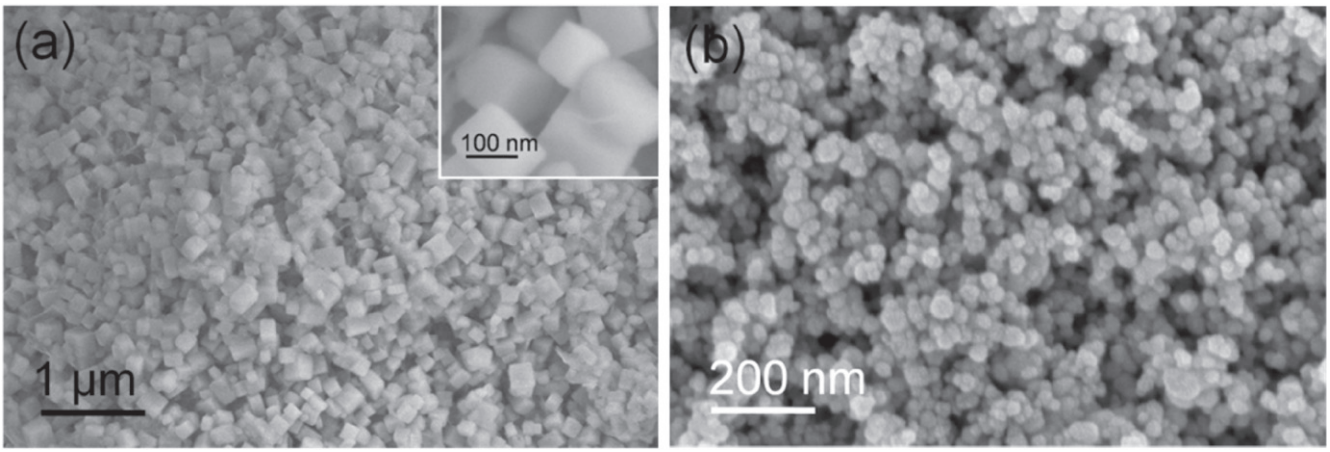

Figure 1. SEM images of (a) $In(OH)_3$ nanocubes and (b) In_2O_3 NPs. Inset of (a) shows a corresponding magnified image.

SAED pattern (figure 2(d), upper inset). The diffraction spots on the ring suggest the considerable single crystallinity of the individual NP. The lattice image shown as a lower inset in figure 2(d) suggests the formation of crystalline In_2O_3 with a lattice spacing of 2.86 Å for (222) planes of In_2O_3. Unlike the present case, Du *et al* reported an unchanged size and morphology of In_2O_3 microcubes upon calcining at 500 °C for 4 h, which could be due to the larger size (>500 nm) of cubes [17]. Further increasing the annealing temperature to 600 °C for 1 h in air, almost all the nanocubes were broken down to In_2O_3 NPs (figure 2(e)). The magnified TEM (figure 2(f)), HRTEM image (figure 2(f), lower inset), and SAED pattern (figure 2(f), upper inset) confirm the crystalline nature of In_2O_3 NPs. In addition, the diameter of In_2O_3 NPs is found to increase to >10 nm. Upon annealing the $In(OH)_3$ nanocubes in air at 750 °C for 1 h, not only was the diameter of In_2O_3 NPs increased to a range of 20−50 nm but also a number of voids were found inside the NPs as shown in the TEM images (figures 2(g) and (h)). The smaller NPs (diameter <30 nm) mostly possess single voids, whereas the slightly bigger NPs (diameter >30 nm) possess multiple voids. The diameter of these voids was measured to be 5−10 nm. The continuous lattice pattern in the HRTEM image (figure 2(i)) of In_2O_3 NPs with a spacing of 4.05 Å corresponding to a (211) plane indicates the highly crystalline nature of the NPs. The spot SAED further confirms the single crystalline nature of In_2O_3 NPs.

3.2. Structural properties

The crystal structure of the as-synthesized samples was measured using powder x-ray diffraction (XRD). Figure 3(a) shows the XRD pattern of the $In(OH)_3$ nanocubes. The intense diffraction features indicate the crystalline nature of the sample. All the diffraction features in the XRD pattern of $In(OH)_3$ (figure 3(a)) are indexed and match the cubic phase of $In(OH)_3$ with a lattice constant of $a = 0.797$ nm, which is in good agreement with the standard data file (JCPDS No. 01-085-1338). No other phases and/or impurities, such as InOOH or In_2O_3, were detected indicating the high purity of the sample. Similarly, the diffraction features of the 400, 500, and 750 °C calcined samples (figures 3(b)−(c)) were indexed matching the cubic In_2O_3 with a lattice constant of $a = 1.012$ nm (JCPDS No. 00-006-0416). Impurity phases, such as indium and/or $In(OH)_3$, were not detected. The increase in diffraction intensity with a decrease in the full-width-half-maximum of the most intense (222) diffraction peak of In_2O_3 suggests an improvement in the crystallinity with calcination temperature.

3.3. Surface composition

The surface composition and chemical states of the as-synthesized $In(OH)_3$ nanocubes and In_2O_3 NPs obtained by calcining nanocubes at 750 °C for 1 h in air were analyzed by XPS. The survey spectra (figure S3, SI) of both the samples show the presence of In and O along with C as surface impurities. The position of the XPS peaks is calibrated to C 1s binding energy (BE) at 284.5 eV. Figures 4(a) and (b) show the In 3d and O 1s region XPS spectra of $In(OH)_3$ nanocubes, respectively. The In 3d features are found to be asymmetric and therefore deconvoluted using CASA XPS. The prominent photoelectron features at 445.5 eV and 453.1 eV are assigned as In $3d_{5/2}$ and In $3d_{3/2}$ of $In(OH)_3$, respectively. The peaks at BE of 443.6 eV and 451.2 eV can be assigned to In $3d_{5/2}$ and In $3d_{3/2}$ of In_2O_3 respectively [37]. The O 1s feature of In $(OH)_3$ nanocubes shows a prominent peak at 532.1 eV (figure 4(b)), which is assigned to the hydroxyl species of In $(OH)_3$, whereas a less intense peak at 530.1 eV could be due to oxide (In_2O_3) or surface adsorbed oxygen. The detection of oxide species (i.e. In_2O_3 XPS features) on the surface of In $(OH)_3$ nanocubes can be attributed to the bombardment of high-energy x-rays on the specimen allowing the partial dehydration of $In(OH)_3$ [37]. This dehydration process is further assisted by the high vacuum environment used in the XPS measurement. Moreover, both the In 3d and O 1s XPS peak intensity for $In(OH)_3$ is much higher than that for In_2O_3 suggesting that the nanocubes are indeed $In(OH)_3$ as confirmed by XRD analysis. Figure 4(c) shows the In $3d_{5/2}$ and In $3d_{3/2}$ features of In_2O_3 NPs at 443.8 eV and 451.3 eV,

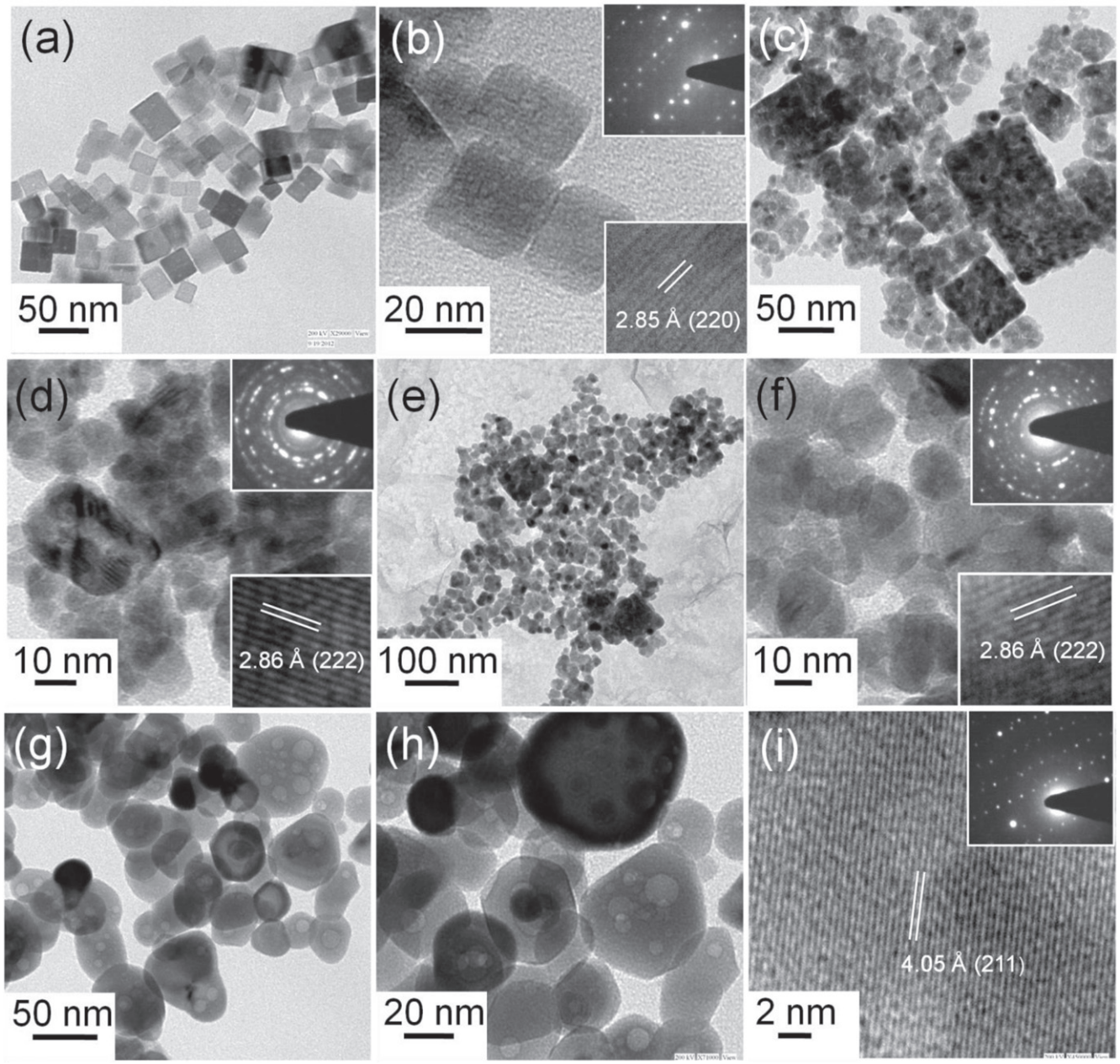

Figure 2. TEM images of (a), (b) $In(OH)_3$ nanocubes, and $In(OH)_3$ nanocubes calcined at (c), (d) 500 °C, (e), (f) 600 °C and (g)–(i) 750 °C for 1 h in air. Insets of (b)–(f) and (i) show the corresponding SAED pattern and/or HRTEM image.

respectively, matching well the literature values for In_2O_3 [38]. The O 1s features of In_2O_3 NPs are found at 529.1 eV and 531.2 eV (figure 4(d)), which can be assigned to the oxide and surface adsorbed oxygen/hydroxyl group, respectively.

3.4. Thermal stability

A thermogravimetry (TG) measurement was performed in atmospheric air in order to understand the thermal conversion of $In(OH)_3$ nanocubes to In_2O_3 NPs. Figure 5 shows the TG plot and corresponding derivative plot. The weight loss of 16.1% in the temperature range of 100 to 400 °C matches the theoretical values of 16.3% for the transformation of $In(OH)_3$ to In_2O_3, which is in accordance with the previous reports [21, 39]. Moreover, the dominant weight loss begins at ~200 °C and ends at 300 °C as shown in figure 5. This weight loss further supports the XRD results (figure 3(b)) on the formation of In_2O_3 phase by calcining $In(OH)_3$ nanocubes at 400 °C for 1 h in air.

3.5. Optical properties

Figures 6(A) and (B) show the UV–vis spectra and corresponding band gap plots for $In(OH)_3$ nanocubes and In_2O_3 NPs, respectively. The sharp decrease in the transmittance (T) at ~210 nm suggests a large band gap for $In(OH)_3$ nanocubes

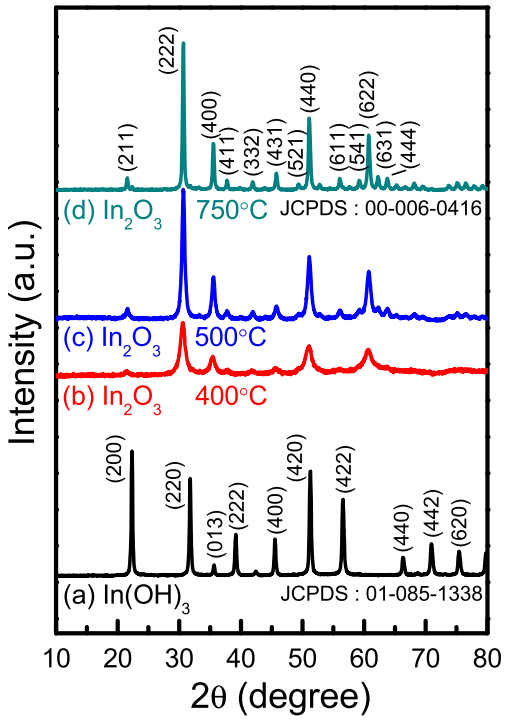

Figure 3. XRD patterns of (a) $In(OH)_3$ nanocubes and (b)–(d) In_2O_3 NPs obtained by calcining the as-synthesized $In(OH)_3$ nanocubes at (b) 400, (c) 500, and (d) 750 °C for 1 h in air.

(figure 6(A)). The decrease in transmittance for In_2O_3 NPs occurs at a much higher wavelength of ~550 nm, indicating a smaller band gap than that of $In(OH)_3$ nanocubes. The zero-crossing values obtained by the extrapolation of a linear fit to the rising edges of the respective $((-\ln T) \times h\nu)^2$ versus photon energy ($h\nu$) plots (figure 6(B)) were taken as the band gap of the material. The estimated band gaps of $In(OH)_3$ nanocubes and In_2O_3 NPs are 5.18 and 2.7 eV, respectively. These values match well with the reported values for $In(OH)_3$ and In_2O_3 [40].

3.6. Growth mechanism of $In(OH)_3$ nanocubes and In_2O_3 NPs

The possible formation mechanism of In_2O_3 NPs can be described by a two-step process. In the first step, $In(OH)_3$ nanocubes were formed by a hydrolysis reaction of In^{3+} and L-arginine under hydrothermal conditions at 200 °C for 6 h. Since L-arginine possesses the amine groups (=NH− and −NH_2) and acid group (−COOH), it acts both as a reducing and a shape-controlling agent. Thus L-arginine plays a similar role to that of the CTAB, sodium borohydride, amines (ethylenediamine, ethylamine, L-proline, and ammonia solution), acetic acid, and oleic acid previously used for the synthesis of $In(OH)_3$ nanocubes [10–12]. For comparison, synthesis was also performed in the absence of L-arginine keeping the rest of the parameters fixed (reaction temperature 200 °C for 6 h). Figures S4(a), (b) in the SI show the cube-shaped $In(OH)_3$ particles of a much larger size (>1 μm). The role of L-arginine is thus found to not only control the formation of uniform $In(OH)_3$ nanocubes but also those of a much smaller size (<150 nm) as discussed earlier (figures 1(a) and 2(a)). Upon calcining at 750 °C for 1 h, the microcubes obtained without L-arginine are found to have transformed into irregularly shaped In_2O_3 particles (phase was confirmed by powder XRD) as shown in figures S4(c) and (d). Moreover, multiple voids are found in this case, like that of the In_2O_3 NPs obtained by calcining $In(OH)_3$ nanocubes obtained with L-arginine. In the second step, In_2O_3 NPs were obtained by calcining as-synthesized $In(OH)_3$ nanocubes. Figure 7 illustrates the schematics of the product obtained by calcining $In(OH)_3$ nanocubes at a different temperature. The morphology of $In(OH)_3$ nanocubes (figure 7(a)) remains the same after calcination at 400 °C for 1 h in air. However, calcination at 500 °C in air for 1 h produced nanocubes composed of NPs and individual NPs (figure 7(b)). Although the cube shape remains for the nanocubes with a size larger than 50 nm across the diagonal, they are found to be composed of NPs, i.e. single crystalline $In(OH)_3$ nanocubes become polycrystalline In_2O_3. On the other hand, smaller cubes (<50 nm) are fragmented into finer NPs with a diameter of <10 nm. However, Du *et al* reported no change in the morphology of $In(OH)_3$ nanocubes upon calcination at 500 °C for 4 h, which could be due to the larger size (>500 nm) of cubes. Upon calcining at 600 °C for 1 h, all the $In(OH)_3$ nanocubes are broken down into spherical In_2O_3 NPs (figure 7(c)). This coincides with an increase in the diameter of the NPs to 10−20 nm due to the well-known grain growth phenomenon. A further increase in the calcination temperature to 750 °C not only increases the diameter but also causes voids to appear inside the NPs (figure 7(d)). The specific surface area of the as-synthesized $In(OH)_3$ nanocubes and In_2O_3 NPs obtained by calcining at 750 °C is measured using a N_2 adsorption-desorption study. Figures S5(a) and S5(b) show the adsorption-desorption isotherm and corresponding Barrett–Joyner–Halenda (BJH) plots, respectively. The specific surface area of $In(OH)_3$ nanocubes and In_2O_3 NPs are estimated to be 21.36 $m^2\,g^{-1}$ and 84.035 $m^2\,g^{-1}$, respectively. The higher BET surface area of In_2O_3 NPs correlates to its morphology shown above. In addition, BJH analysis suggests the formation of fine pores with a size in the range of 2−3 nm in the case of In_2O_3 NPs.

The formation of voids can be described by the Kirkendall effect. As per the Kirkendall effect, pore/void formation occurs because of the difference in the diffusion rates of two components in a diffusion couple [41]. Such effects have been demonstrated with several examples, including the formation of hollow nanocrystals of CoO, Pb@PbS, Pb@Ag, FePt@CoS_2, and Fe_3O_4 [41–44]. This effect can occur via the cation or anion exchange process. In the present study, the calcination of $In(OH)_3$ nanocubes in air converts its surface to In_2O_3. Anion exchange can thus occur, i.e. outward diffusion of core OH^- [of $In(OH)_3$] and exchange with surface O^{2-} (of In_2O_3). This leads to the formation of voids/pores inside the particle, which can be described on the basis of the thermal stability and diffusion rate of anions. At a higher calcination temperature, the surface of $In(OH)_3$ first turns to In_2O_3 by the evaporation of water molecules. As the thermal stability of $In(OH)_3$ is lower than that of In_2O_3, the In−OH bond is

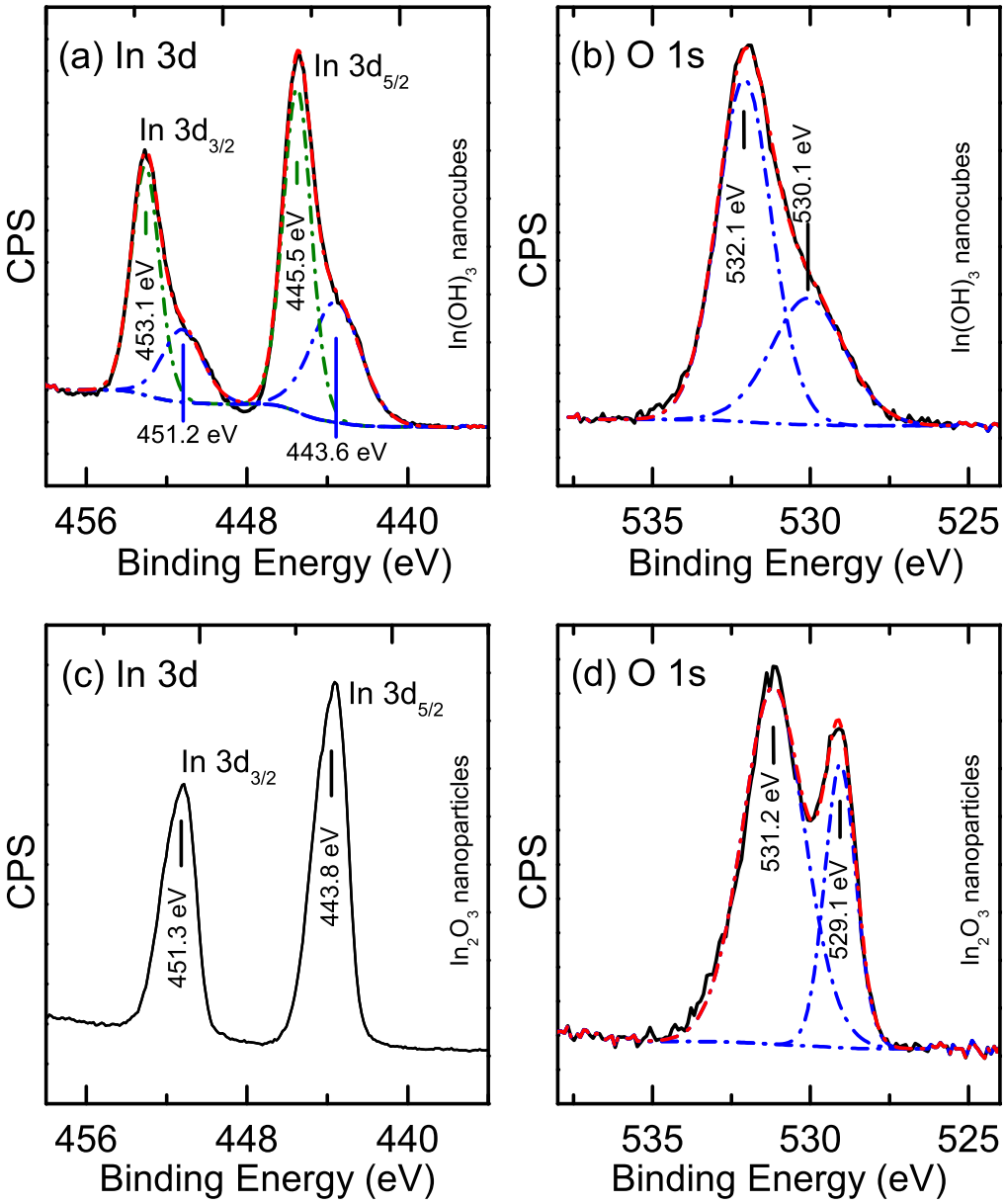

Figure 4. Region XPS spectra of (a), (b) $In(OH)_3$ nanocubes and (c), (d) In_2O_3 NPs. (a)–(c) In 3d and (b), (d) O 1s region spectra.

expected to first break down at a lower temperature. In addition, the diffusion rate of OH^- ions is higher than that of O^{2-} due to the smaller radii of the former (137 pm) than the latter (140 pm) [16]. Thus, the OH^- ions would move outward at a faster rate than the inward movement of O^{2-} ions preventing the anion exchange from occurring. This leads to the sudden creation of large numbers of vacancies in the core of the particle forming voids or pores. It is important to note that the NPs with voids formed via anion exchange accompanied by the nanoscale Kirkendall effect generally preserve their shape, as found in the present study. In addition, the single crystalline nature of NPs remained, which has not widely been found [45–47]. The number of voids forming is also found to be directly dependent on the diameter of the NPs in the present case, and multiple voids are found in NPs with a diameter greater than 20 nm.

3.7. Photocatalytic activity

The photocatalytic activities of as-prepared $In(OH)_3$ cubes and In_2O_3 particles (obtained in the presence and absence of L-arginine) are evaluated in terms of the degradation of rhodamin B (RhB) and alizarin red S (ARS) dye in aqueous solution (10^{-5} mol L^{-1}) under 365 nm UV or visible light. The photocatalytic activity of standard P-25 TiO_2 NPs of diameter ~21 nm is also tested for comparison under both UV and visible light irradiation. Prior to irradiation, catalyst powder was dispersed in the dye solution for 1 h in the dark to saturate the surface adsorption and desorption of dye molecules on the catalyst surface. The initial adsorption of RhB/ARS on the surface of $In(OH)_3$ and In_2O_3 was found to be saturated within 1 h as shown in figure 8. Adsorption of RhB (12%) was almost the same with $In(OH)_3$ and In_2O_3 after 1 h

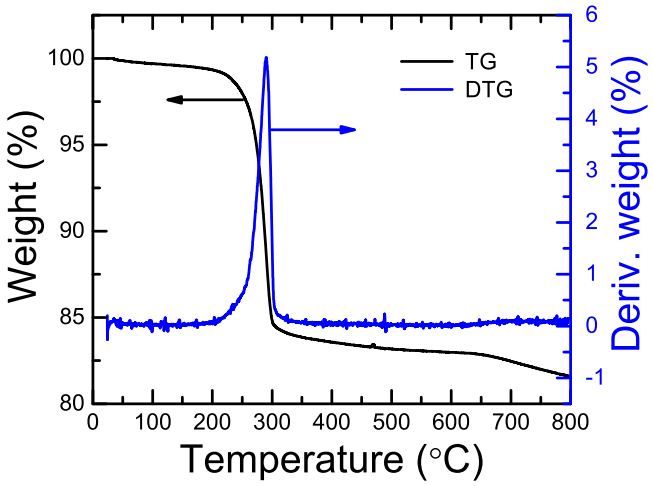

Figure 5. TG and differential TG (DTG) plots of $In(OH)_3$ nanocubes showing their transformation to In_2O_3 upon heating to 400 °C with a weight loss of 16.1%.

in the dark. On the other hand, adsorption of ARS on In_2O_3 (35%) is found to be much higher than that of $In(OH)_3$ (11%) in the dark. This is believed to be due to the nature of the dyes and their electrostatic interaction with the NPs. Similar adsorption properties are found with P-25 TiO_2 NPs. Figures S6(a) and S6(b) show the typical UV–vis absorption spectra of a RhB solution irradiated by UV light for different durations in the presence of $In(OH)_3$ nanocubes and In_2O_3 NPs, respectively. The characteristic absorption of RhB at $\lambda = 553$ nm is selected to monitor the photocatalytic degradation process. Figure 8 shows the degradation profile i.e. plot of C/C_0 versus irradiation time 't', where C_0 and C are the dye concentration before and after the irradiation time of t. No degradation of dyes was observed in the absence of a catalyst. After 12% surface adsorption in the dark, approximately 36% and 88% of the RhB is degraded in the presence of $In(OH)_3$ and In_2O_3 in 4 h under UV light, respectively (figure 8(a)). Although a similar trend was observed for ARS (figure 8(b)), photodegradation was found to be incomplete even after 4 h. Figure 8(b) shows that photodegradation is saturated in 3 h of UV irradiation, with ~37% and 11% of ARS remaining present in the solution in the presence of $In(OH)_3$ and In_2O_3, respectively. For comparison, the photocatalytic activity of P-25 TiO_2 was tested. After an initial 16% surface adsorption in the dark, 69% of RhB is degraded with P-25 TiO_2 under light in 4 h, which is much lower than that of In_2O_3 NPs. On the other hand, surface adsorption of ARS in the dark and its degradation under UV light with P-25 TiO_2 is almost the same as that of In_2O_3 NPs. In addition, the photocatalytic activity of $In(OH)_3$ microcubes obtained in the absence of L-arginine is studied and found to be negligible (not shown). The In_2O_3 particles obtained by annealing $In(OH)_3$ microcubes also showed poor photocatalytic activity because of their much larger size and agglomeration (figure S4), as shown in figure 8. As the band gap of In_2O_3 falls in the visible region (2.7 eV, figure 6), we have measured the photocatalytic performance of In_2O_3 NPs for the degradation of RhB and ARS under visible light. After 13% (16%) initial adsorption in the dark, 35% (19%) of RhB is found to have degraded under visible light in the presence of In_2O_3 (P-25 TiO_2) NPs. Similarly, degradation of ARS was higher with In_2O_3 NPs than that of P-25 TiO_2 under visible light. Moreover, the degradation performance of RhB/ARS under visible light was lower than that of UV light. This is because of the incomplete use of the visible light spectrum (i.e. light below the band gap energy of the catalyst) for the creation of $e^- - h^+$ pairs in the semiconductor catalyst. Moreover, the present study confirms the superior photodegradation ability of In_2O_3 NPs toward RhB and ARS. This could be explained on the basis of a smaller band gap and smaller size (larger surface area) of In_2O_3 NPs than that of $In(OH)_3$ nanocubes. Previously, Yin *et al* reported a ~92% RhB degradation in 240 min with rhombohedral In_2O_3 nanocrystals of diameter 10−30 nm [16]. The present result suggests that the photodegradation performance of cubic In_2O_3 NPs (diameter 20−50 nm) is higher than that of rhombohedral In_2O_3.

The photocatalytic degradation mechanism of RhB/ARS in the present system under UV–vis light irradiation can be described based on the well-known $e^- - h^+$ formation, their separation in the semiconductor and involvement in the formation of reactive species for the degradation of organic contaminants [15, 48]. The use of visible light creates a smaller number of $e^- - h^+$ pairs because light with a wave length below the band gap energy is not absorbed by the semiconductor catalyst and thereby the photocatalytic activity is poorer compared to the UV light. The following are the reaction steps primarily involved in the degradation of organic contaminants (dyes) on the semiconductor surface [49].

$$\text{Semiconductor(SC) i.e. } In(OH)_3/In_2O_3 + \text{light}(h\nu) \rightarrow SC_{VB}\left(h^+\right) + SC_{CB}\left(e^-\right) \quad (1)$$

$$H_2O + SC_{VB}\left(h^+\right) \rightarrow {}^{\bullet}OH^{\cdot} + H^+ + SC \quad (2)$$

$$O_2 + SC_{CB}\left(e^-\right)^{\cdot} \rightarrow {}^{\bullet}Q_2^- + SC \quad (3)$$

$${}^{\bullet}Q_2^- + H^+ \rightarrow HO_2^{\bullet} \quad (4)$$

$${}^{\bullet}O_2^- \text{ or } {}^{\bullet}OH \text{ or } h^+ + \text{adsorbed dye} \rightarrow \text{degraded products} \quad (5)$$

The radicals (${}^{\bullet}OH$, ${}^{\bullet}O_2^-$, and $HO_2^{\bullet}$) formed as shown in the above reactions are the prime reactive species for the degradation of organic substrates on the semiconductor surface. As these heterocatalytic reactions occur on the surface of semiconductors, the surface area of the catalyst plays a crucial role in the photocatalysis. In addition to the smaller band gap, the larger surface area of In_2O_3 NPs is thus another important factor in its higher photocatalytic activity.

3.8. CO Oxidation activity

Figure 9 displays the CO oxidation activities over $In(OH)_3$ nanocubes and In_2O_3 NPs (obtained at 750 °C) as a function of reaction temperatures. The CO conversion (%) as shown in the Y-axis of figure 9 was calculated using the equation $\{([CO]_{in} - [CO]_{out})/[CO]_{in}\} \times 100$. In the first and second CO oxidation runs of $In(OH)_3$ nanocubes, the oxidation onset

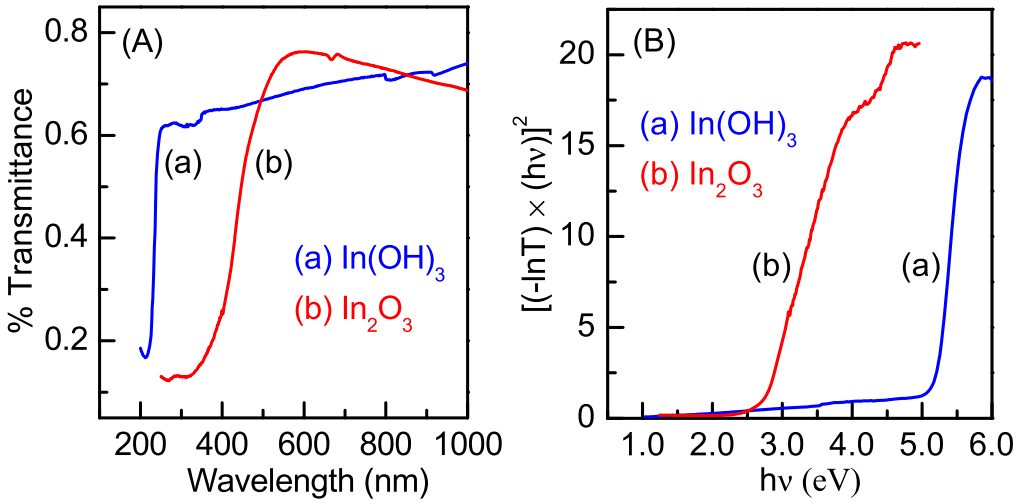

Figure 6. (A) UV–vis spectra of (a) $In(OH)_3$ nanocubes and (b) In_2O_3 NPs and the corresponding (B) band gap plots of $[(-\ln T) \times (h\nu)]^2$ as a function of $h\nu$.

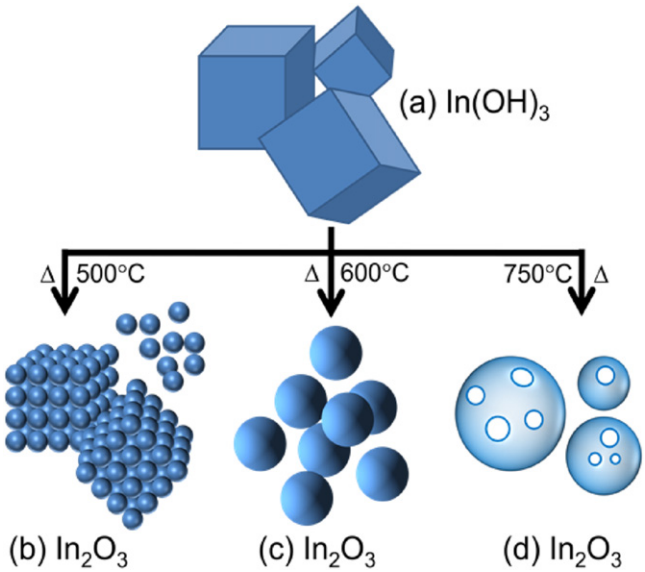

Figure 7. Schematics on the morphology transformation of $In(OH)_3$ nanocubes to In_2O_3 NPs by calcining $In(OH)_3$ nanocubes at 500, 600, and 750 °C for 1 h in air.

(T_{onset}) appeared at 355 °C. However, the $T_{10\%}$ (the temperature at 10% CO conversion) was found at 545 °C and 410 °C in the first and second runs, respectively. The ($T_{10\%}-T_{onset}$) was found to be only 55 °C for the second run, which is significantly smaller than the 190 °C for the first run. This indicates that the second run has reached $T_{10\%}$ earlier, i.e. at a lower temperature. The significant difference is mainly due to the transformation of $In(OH)_3$ into In_2O_3. In the first CO oxidation run of $In(OH)_3$ nanocubes, a H_2O signal was detected (figure S7, SI). This is due to the dehydration of $In(OH)_3$ forming In_2O_3 (discussed above with the TG data). As expected, the water evolution starts at ~200 °C and ends at ~400 °C with complete transformation of $In(OH)_3$ into In_2O_3. In the second CO oxidation run of $In(OH)_3$ nanocubes, and in the first and second runs of In_2O_3 NPs, we detected no H_2O signals (figure S7). For the powder In_2O_3 NP samples, the CO oxidation onsets were observed at 415 °C and 325 °C in the first and second runs, respectively, as shown in figure 9. The onset temperature of 325 °C in the second run is comparable to that of previously reported In_2O_3 wires but better (i.e. at a lower temperature) than that of cube-, donut-, and plate-shaped In_2O_3 [35]. The $T_{10\%}$ with In_2O_3 NPs was found at 500 °C and 375 °C in the first and second runs, respectively. Based on the $T_{10\%}$ values in the second runs, the CO oxidation in In_2O_3 NPs occurs at a temperature 35 °C lower as compared to $In(OH)_3$ nanocubes. This suggests In_2O_3 NPs are a promising material for CO oxidation.

4. Conclusions

In summary, we have successfully synthesized cubic $In(OH)_3$ nanocubes and In_2O_3 NPs using a biomolecule-assisted hydrothermal method. L-arginine is demonstrated to successfully synthesize indium-based nanomaterials. The present synthesis method does not utilize any toxic or hazardous chemicals, and the formation of $In(OH)_3$ nanocubes is demonstrated following a shorter hydrothermal reaction duration of 6 h. Upon calcining $In(OH)_3$ nanocubes at different temperatures in air, we present the morphology transformation of $In(OH)_3$ nanocubes to In_2O_3 NPs with voids through a detailed TEM study. The formation of voids inside In_2O_3 NPs is explained on the basis of the Kirkendall effect following anion exchange, i.e. exchange of surface O^{2-} with core OH^-. We compare the photocatalytic activity of both $In(OH)_3$ nanocubes and In_2O_3 NPs for the degradation of RhB and ARS under UV and visible light irradiation. The photocatalytic activity of In_2O_3 NPs was measured to be much higher than that of $In(OH)_3$ nanocubes due to its smaller band gap and porous structure. Furthermore, the CO oxidation activity i.e. $T_{10\%}$ (the temperature at 10% CO conversion) for In_2O_3 was found at 375 °C, which is 35 °C lower than that

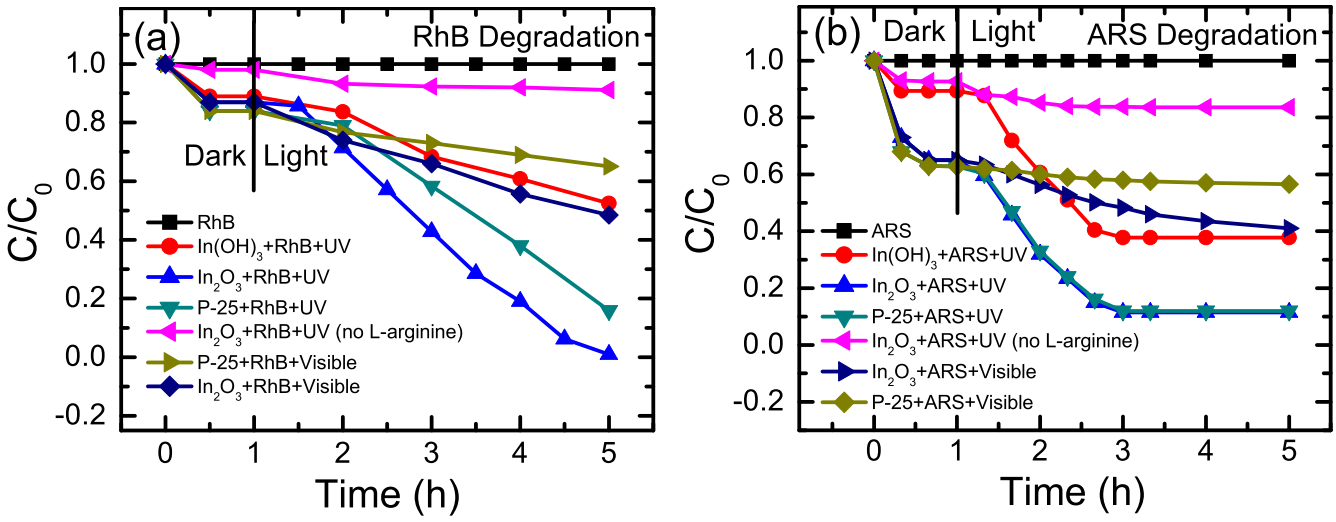

Figure 8. The UV and visible light-assisted degradation of (a) RhB and (b) ARS with $In(OH)_3$ nanocubes and In_2O_3 NPs obtained by calcining $In(OH)_3$ nanocubes at 750 °C for 1 h in air. No degradation of RhB and ARS was found in the absence of a catalyst. For comparison, the photocatalytic activity of In_2O_3 obtained by calcining $In(OH)_3$ microcubes obtained without L-arginine and P-25 TiO_2 NPs is also shown.

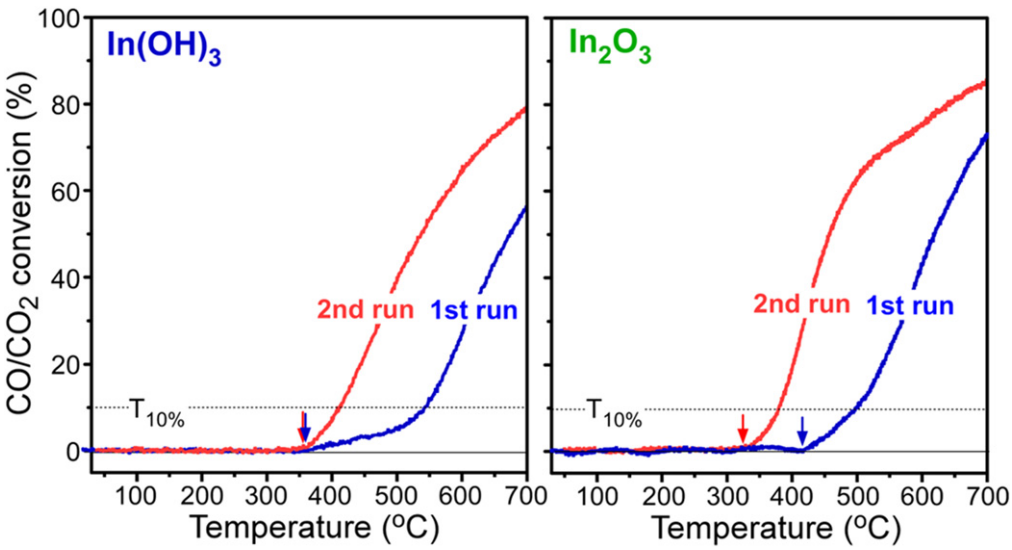

Figure 9. First and second run temperature programmed for CO oxidation (i.e. CO to CO_2 conversion (%)) profiles for (left) $In(OH)_3$ nanocubes and (right) In_2O_3 NPs obtained by calcining $In(OH)_3$ nanocubes at 750 °C for 1 h in air.

measured for $In(OH)_3$ nanocubes at 410 °C. This suggests a higher CO oxidation performance of In_2O_3 than that of $In(OH)_3$. The present green synthesis of nanomaterials and their application for the removal of organic pollutants in water and CO in air have strong implications for future environmental remediation.

Supporting information

TEM images, survey XPS spectra of $In(OH)_3$ nanocubes and In_2O_3 NPs, nitrogen adsorption-desorption isotherm, UV–vis absorption plots of RhB as a function of irradiation time

Acknowledgments

This work was supported by the Science and Engineering Research Board (SERB), New Delhi, India through the grant SB/S1/IC-15/2013 and the National Research Foundation of Korea (NRF) grant funded by the Korean government (MEST) (NRF-2014R1A1A2055923).

References

[1] Zhuiykov S 2014 *Nanostructured Semiconductor Oxides for the Next Generation of Electronics and Functional Devices: Properties and Applications* (New Delhi: Woodhead)

[2] Wang Z L 2004 Zinc oxide nanostructures: growth, properties and applications *J. Phys.: Condens. Matter* **16** R829

[3] Roy N, Park Y, Sohn Y, Leung K T and Pradhan D 2014 Green synthesis of anatase TiO_2 nanocrystals with diverse shapes and their exposed facets-dependent photoredox activity *ACS Appl. Mater. Interfaces* **6** 16498–507

[4] Gurlo A, Ivanovskaya M, Bârsan N, Schweizer-Berberich M, Weimar U, Göpel W and Diéguez A 1997 Grain size control in nanocrystalline In_2O_3 semiconductor gas sensors *Sensors Actuators* B **44** 327–33

[5] Caldorera-Moore M, Guimard N, Shi L and Roy K 2010 Designer nanoparticles: incorporating size, shape, and triggered release into nanoscale drug carriers *Expert Opin. Drug Deliv.* **7** 479–95

[6] Im J-H, Jang I-H, Pellet N, Grätzel M and Park N-G 2014 Growth of $CH_3NH_3PbI_3$ cuboids with controlled size for high-efficiency Perovskite solar cells *Nat. Nanotechnology* **9** 927–32

[7] Das D, Chaudhuri S and Maji S 2008 Ethanol−water mediated solvothermal synthesis of cube and pyramid shaped nanostructured tin oxide *J. Phys. Chem.* C **112** 6213–9

[8] Niederberger M 2007 Nonaqueous sol-gel routes to metal oxide nanoparticles *Acc. Chem. Res.* **40** 793–800

[9] Pradhan D and Leung K T 2009 Template-free single-step electrochemical synthesis of ZnO hollow nanospheres: self-assembly of hollow nanospheres from nanoparticles *J. Mater. Chem.* **19** 4902–5

[10] Yan T, Long J, Shi X, Wang D, Li Z and Wang X 2010 Efficient photocatalytic degradation of volatile organic compounds by porous indium hydroxide nanocrystals *Environ. Sci. Technol.* **44** 1380–5

[11] Yan T, Wang X, Long J, Liu P, Fu X, Zhang G and Fu X 2008 Urea-based hydrothermal growth, optical and photocatalytic properties of single-crystalline $In(OH)_3$ nanocubes *J. Colloid Interface Sci.* **325** 425–31

[12] Cao H, Zheng H, Liu K and Fu R 2009 Single-crystalline semiconductor $In(OH)_3$ nanocubes with bifunctions: superhydrophobicity and photocatalytic activity *Cryst. Growth Des.* **10** 597–601

[13] King P D C *et al* 2009 Band gap, electronic structure, and surface electron accumulation of cubic and rhombohedral In_2O_3 *Phys. Rev.* B **79** 205211

[14] Fuchs F and Bechstedt F 2008 Indium-oxide polymorphs from first principles: quasiparticle electronic states *Phys. Rev.* B **77** 155107

[15] Talebian N and Nilforoushan M R 2010 Comparative study of the structural, optical and photocatalytic properties of semiconductor metal oxides toward degradation of methylene blue *Thin Solid Films* **518** 2210–5

[16] Yin J and Cao H 2012 Synthesis and photocatalytic activity of single-crystalline hollow rh-In_2O_3 nanocrystals *Inorg. Chem.* **51** 6529−6536

[17] Du J, Yang M, Cha S N, Rhen D, Kang M and Kang D J 2008 Indium hydroxide and indium oxide nanospheres, nanoflowers, microcubes, and nanorods: synthesis and optical properties *Cryst. Growth Des.* **8** 2312–7

[18] Gurlo A, Barsan N, Weimar U, Ivanovskaya M, Taurino A and Siciliano P 2003 Polycrystalline well-shaped blocks of indium oxide obtained by the sol-gel method and their gas-sensing properties *Chem. Mater.* **15** 4377–83

[19] Yang J, Lin C, Wang Z and Lin J 2006 $In(OH)_3$ and In_2O_3 nanorod bundles and spheres: microemulsion-mediated hydrothermal synthesis and luminescence properties *Inorg. Chem.* **45** 8973–9

[20] Chen C, Chen D, Jiao X and Chen S 2007 In_2O_3 nanocrystals with a tunable size in the range of 4–10 nm: one-step synthesis, characterization, and optical properties *J. Phys. Chem.* C **111** 18039–43

[21] Liu X, Zhou L, Yi R, Zhang N, Shi R, Gao G and Qiu G 2008 Single-crystalline indium hydroxide and indium oxide microcubes: synthesis and characterization *J. Phys. Chem.* C **112** 18426–30

[22] Chen L-Y, Zhang Z-D and Wang W-Z 2008 Self-assembled porous 3D flowerlike (β-In_2S_3 structures: synthesis, characterization, and optical properties *J. Phys. Chem.* C **112** 4117–23

[23] Chen L-Y and Zhang Z-D 2008 Biomolecule-assisted synthesis of $In(OH)_3$ hollow spherical nanostructures constructed with well-aligned nanocubes and their conversion into C-In_2O_3 *J. Phys. Chem.* C **112** 18798–803

[24] Nayak A K, Lee S, Sohn Y and Pradhan D 2014 Synthesis of In_2S_3 microspheres using a template-free and surfactant-less hydrothermal process and their visible light photocatalysis *Cryst. Eng. Commun.* **16** 8064–72

[25] Shao Y, Jin Y D and Dong S J 2004 Synthesis of gold nanoplates by aspartate reduction of gold chloride *Chem. Commun.* 1104–5

[26] Yang J H, Lu L H, Wang H S, Shi W D and Zhang H J 2006 Glycyl Glycine Templating Synthesis of Single-Crystal Silver Nanoplates *Cryst. Growth Des.* **6** 2155–8

[27] Sasaki T, Nakaya M, Kanie K and Muramatsu A 2009 Amino acid assisted hydrothermal synthesis of $In(OH)_3$ nanoparticles controlled in size and shape *Mater. Trans.* **50** 2808–12

[28] Duan L, Jia S, Wang Y, Chen J and Zhao L 2009 Synthesis of Fe_3O_4 polyhedra by hydrothermal method: using L-arginine as precipitator *J. Mater. Sci.* **44** 4407–12

[29] Hu B, Wang S-B, Wang K, Zhang M and Yu S-H 2008 Microwave-assisted rapid facile 'green' synthesis of uniform silver nanoparticles: self-assembly into multilayered films and their optical properties *J. Phys. Chem.* C **112** 11169–74

[30] Talwatkar S S, Tamgadge Y S, Sunatkari A L, Gambhire A B and Muley G G 2014 Amino acids (L-arginine and L-alanine) passivated CdS nanoparticles: synthesis of spherical hierarchical structure and nonlinear optical properties *Solid State Sci.* **38** 42–8

[31] Liu D, Lei W, Qin S, Hou L, Liu Z, Cuid Q and Chen Y 2013 Large-scale synthesis of hexagonal corundum-type In_2O_3 by ball milling with enhanced lithium storage capabilities *J. Mater. Chem.* A **1** 5274−5278

[32] Sharma R, Mane R S, Min S K and Han S-H 2009 Optimization of growth of In_2O_3 nano-spheres thin films by electrodeposition for dye-sensitized solar cells *J. Alloys Compd.* **479** 840−843

[33] Jiang H, Zhao L, Gai L, Ma L, Ma Y and Li M 2013 Hierarchical Rh-In_2O_3 Crystals derived from InOOH counterparts and their sensitivity to ammonia gas *Cryst. Eng. Commun.* **15** 7003−7009

[34] Huang C-Y, Lin G-C, Wu Y-J, Lin T-Y, Yang Y-J and Chen Y-F 2011 Efficient light harvesting by well-aligned In_2O_3 nanopushpins as antireflection layer on Si solar cells *J. Phys. Chem.* C **115** 13083–7

[35] Kim W J, Pradhan D and Sohn Y 2013 Fundamental Nature and CO Oxidation activities of indium oxide nanostructures: 1D-wires, 2D-plates, and 3D-cubes and donuts *J. Mater. Chem.* A **1** 10193–202

[36] Shanmugasundaram A, Ramireddy B, Basak P, Manorama S V and Srinath S 2014 Hierarchical $In(OH)_3$ as a precursor to mesoporous In_2O_3 nanocubes: a facile synthesis route, mechanism of self-assembly, and enhanced sensing response toward hydrogen *J. Phys. Chem.* C **118** 6909−6921

[37] Jean S -T and Her Y -C 2011 Growth mechanism and cathodoluminescence properties of indium hydroxide nanocubes synthesized from a simple aqueous solution *Cryst. Eng. Commun.* **13** 2324–30

[38] Shinde D V, Ahn D Y, Jadhav V V, Lee D Y, Shrestha N K, Lee J K, Lee H Y, Mane R S and Han S -H 2014 A

coordination chemistry approach for shape controlled synthesis of indium oxide nanostructures and their photoelectrochemical properties *J. Mater. Chem.* A **2** 5490–8

[39] Wu Q, Chen J, Zhang F, Xiao P, Lu Y, Wang X and Hu Z 2012 Anion-induced morphological regulation of $In(OH)_3$ nanostructures and their conversion into porous In_2O_3 derivatives *Cryst. Eng. Commun.* **14** 3397–403

[40] Avivi S, Mastai Y and Gedanken A 2000 Sonohydrolysis of In^{3+} Ions: formation of needle-like particles of indium hydroxide *Chem. Mater.* **12** 1229–33

[41] Yin Y, Rioux R M, Erdonmez C K, Hughes S, Somorjai G A and Alivisatos A P 2004 Formation of hollow nanocrystals through the nanoscale kirkendall effect *Science* **304** 711–4

[42] Wang Y L, Cai L and Xia Y N 2005 Monodisperse spherical colloids of pb and their use as chemical templates to produce hollow particles *Adv. Mater.* **17** 473–7

[43] Gao J, Liang G, Zhang B, Kuang Y, Zhang X and Xu B 2007 FePt@CoS_2 Yolk-Shell nanocrystals as a potent agent to Kill HeLa Cells *J. Am. Chem. Soc.* **129** 1428–33

[44] Peng S and Sun S 2007 Synthesis and characterization of monodisperse hollow Fe_3O_4 NPs *Angew. Chem. Int. Ed.* **46** 4155–8

[45] Park J, Zheng H, Jun Y and Alivisatos A P 2009 Hetero-epitaxial anion exchange yields single-crystalline hollow NPs *J. Am. Chem. Soc.* **131** 13943–5

[46] Lin M, Zhang J, Boothroyd C, Foo Y L, Yeadon M and Loh K P 2004 Hollowing mechanism of zinc sulfide nanowires in vacuum induced by an atomic oxygen beam *J. Phys. Chem.* B **108** 9631–7

[47] Dloczik L and Konenkamp R 2003 Nanostructure transfer in semiconductors by Ion Exchange *Nano Lett.* **3** 651–3

[48] Park Y, Na Y, Pradhan D, Min B-K and Sohn Y 2014 Adsorption and UV/Visible photocatalytic performance of BiOI for methyl orange, Rhodamine B and methylene blue: Ag and Ti-loading effects *Cryst. Eng. Commun.* **16** 3155–67

[49] Cao H, Xiao Y and Zhang S 2011 The synthesis and photocatalytic activity of ZnSe microspheres *Nanotechnology* **22** 015604–12